

**Importance of the nonlocal exchange potential for effective mass
calculations in semiconductors: Benchmarking
exchange-correlation potentials with the mstar60 dataset**

Magdalena Laurien* and Oleg Rubel†

*Department of Materials Science and Engineering, McMaster University,
1280 Main St W, Hamilton ON L8S 4L8, Canada*

(Dated: November 30, 2021)

arXiv:2111.14772v1 [cond-mat.mtrl-sci] 29 Nov 2021

Abstract

The effective mass is an indicator of the carrier mobility, conductivity and the thermoelectric figure of merit and thus an important parameter in materials design and selection. The accuracy of effective masses predicted by density functional theory depends on the exchange-correlation functional employed, with nonlocal hybrid functionals giving more accurate results than semilocal functionals. In this article, we benchmark the performance of the Perdew–Burke–Ernzerhof, Tran-Blaha modified Becke-Johnson, and the hybrid Heyd-Scuseria-Ernzerhof (HSE) exchange-correlation functionals and potentials to calculate effective masses with perturbation theory. We introduce the `mstar60` dataset which contains 60 effective masses derived from 18 semiconductors. We reveal that the nonlocal exchange in HSE enlarges the optical transition matrix elements leading to the superior accuracy of HSE in the calculation of effective masses. The omission of nonlocal exchange in the transition operator for HSE leads to serious errors. For the semilocal PBE functional, the errors introduced by underestimation of the band gap and of the optical transition matrix elements partially cancel out for the calculation of effective masses. We then compare effective masses of transition metal dichalcogenide bulk and monolayer materials: we show that changes in the matrix elements are important in understanding the layer-dependent effective mass renormalization.

I. INTRODUCTION

The effective mass is an important parameter in materials design and selection. It serves as an indicator of the carrier mobility, conductivity and the thermoelectric figure of merit and is often included in high-throughput computational material studies [1–5]. The effective mass can be obtained from experimental measurements such as cyclotron resonance, Shubnikov-den-Haaf oscillations and angle-resolved photoemission spectroscopy (ARPES).

The effective mass m^* is inversely proportional to the energy band dispersion. In the nearly-free electron model, the energy dispersion of a free electron is described by a parabola: $E = \hbar^2 k^2 / (2m_0)$. In crystalline materials, the electron is no longer free as it interacts with the periodic potential of the ionic lattice. To describe the energy dispersion of the nearly free

* laurienm@mcmaster.ca

† rubelo@mcmaster.ca

electron near a band maximum or minimum of interest in crystalline materials, particularly semiconductors, the mass of the electron m_0 in the parabola is replaced by an effective mass m^* that acts as a scaling term to adjust the band curvature.

The standard procedure for theoretically calculating the effective mass is to fit the band of interest with a parabola or hyperbola and obtain the effective mass from the curvature. An elegant alternative is to use perturbation theory. From perturbation theory, we calculate the inverse effective mass $(m_{\alpha\beta,n}^*)^{-1}$ for non-degenerate bands at a certain k -point as the following [6, Appendix E]

$$\frac{m_0}{m_{\alpha\beta,n}^*} = \delta_{\alpha\beta} + \frac{1}{m_0} \sum_{l \neq n} \frac{p_{nl}^{(\alpha)} p_{ln}^{(\beta)} + p_{nl}^{(\beta)} p_{ln}^{(\alpha)}}{E_n - E_l}, \quad (1)$$

where m_0 is the electron rest mass, α and β indicate directions in Cartesian coordinates (x, y, z) , $\delta_{\alpha\beta}$ is the Kronecker delta, the summation is over the band index l but excludes the band of interest n . E_n and E_l denote the band energies and p_{ln} the optical transition matrix element. The k point index is omitted for simplicity.

This equation helps us to develop some intuition about the factors influencing the effective mass: The larger the interband energy difference term $E_n - E_l$, the less the interaction between the bands contributes to the band dispersion. As a result, the larger the band gap the heavier is normally the effective mass. The larger the matrix element term (the numerator of the sum), the larger the contribution to the band curvature will be. Also, the wavefunctions of two bands can only couple if symmetry selection rules are fulfilled. Otherwise, the transition is not allowed and the matrix element p_{ln} is zero [7, chap. 2.6.1]. For interatomic transitions, i.e. from cation to anion, the effect of the matrix element on the band curvature can be understood in the tight-binding framework [1, 8, 9] and [7, chap. 2.7]. The squared matrix element describes the probability of the transition and is thus related to the two-center hopping or overlap integral of tight-binding theory. Increased overlap between neighboring orbitals leads to greater band dispersion. We should also note that bands lower in energy than n make a positive contribution to the band curvature, while bands higher in energy than n make a negative contribution due to the negative energy difference [7, chap. 2.6.1].

The effective mass of charge carriers can be predicted with density functional theory (DFT) [10] which is a ground-state theory. Still, DFT is commonly used to calculate excited state properties. Density functional approximations using semilocal exchange-correlation

(XC) energy functionals such as the local density or generalized gradient approximation (LDA or GGA) are known to underestimate the band gap of semiconductors significantly [11, chaps. 6.3.1, 9.2.4]. This leads to errors in the band curvature and effective masses. Corrections from many-body theory change the band dispersion [11, chap. 16.1.3] and thus also cause an effective mass renormalization for many materials.

The most obvious renormalization after the band gap correction comes from a relative change in the interband energy difference term $E_n - E_l$ in Eq. (1). This has recently been illustrated for InSe with LDA and *GW* calculations, where Li and Giustino [12] showed that the out-of-plane electron effective mass was corrected three times more strongly than the in-plane mass for quasiparticles calculations. This effect was explained by symmetry selection rules that ruled out a transition matrix element p_{cv} between conduction and the valence band edge for the in-plane mass thus engaging deeper valence states ($p_{c,v-1}$) whose energy position relative to the conduction band edge is less affected by the correction of the fundamental band gap. However, what remains overlooked in Ref. 12 is that not only the band gap but also the p_{ln} matrix elements are renormalized as we transition from LDA to a higher level of theory. The latter will be a central topic of this paper.

To predict more accurate effective masses with DFT we should first find ways to inexpensively correct the band gap. This can be done using the semilocal Tran-Blaha modified Becke-Johnson exchange-correlation potential (TB-mBJ) [13, 14]. Interestingly, effective masses obtained with TB-mBJ are consistently heavier than the experimental result [8, 15–17]. The more expensive hybrid functionals used to correct the band gap, on the other hand, also result in excellent agreement of effective masses with experiment [8]. Kim *et al.* [8] alluded that to obtain correct effective masses, corrections beyond a semilocal potential will ultimately be required. If the band gap is almost correct in TB-mBJ, then the transition matrix element must be underestimated. The role of the matrix element p_{ln} for the renormalization of calculated effective masses has not yet been investigated in detail.

In this work, we benchmark the accuracy of effective masses calculated with several exchange-correlation potentials for a new dataset that we call **mstar60**. Our dataset comprises standard sp-semiconductors, d-semiconductors and monolayer materials. Effective masses are calculated with a perturbation theory approach. We show the extent of renormalization of effective masses caused by changes in the transition matrix elements. We explain the role of the nonlocal exchange potential V_x^{NL} concerning these renormalization

effects. On average 30% heavier masses are predicted with the hybrid functional if incorrect transition matrix elements—that do not include V_x^{NL} —are used.

II. OPTICAL TRANSITION MATRIX ELEMENTS

For the calculation of optical properties, the nonlocality of the potential becomes important when the transition matrix elements are calculated. The matrix elements can be evaluated in the velocity gauge or the length gauge [11, chap. 20.1.1]. Assuming the dipole approximation, the coupling of electrons with an external electromagnetic field is described by $\mathbf{E} \cdot \mathbf{r}$ in the length gauge and $\mathbf{A} \cdot \mathbf{p}$ in the velocity gauge [18, chap. 5-1][19, 20]. Charge conservation and gauge invariance require the equivalence of the two interaction terms [20, 21].

In the length or longitudinal gauge, the position operator \mathbf{r} is used for the calculation of the optical transition matrix elements (in atomic units) [22]

$$p_{nl} = \lim_{q \rightarrow 0} q^{-1} (E_{l, \mathbf{k}+\mathbf{q}} - E_{n, \mathbf{k}}) \langle \psi_{l, \mathbf{k}+\mathbf{q}} | e^{i\mathbf{q}\cdot\mathbf{r}} | \psi_{n, \mathbf{k}} \rangle, \quad (2)$$

where $\psi_{l, \mathbf{k}}$ is the single-particle wavefunction and \mathbf{q} is a small momentum vector shift.

In the velocity gauge (also called transverse or Coulomb gauge) transition matrix elements are calculated from the velocity operator (in atomic units) \hat{v} [23]:

$$p_{nl} = \langle \psi_{l, \mathbf{k}} | \hat{v} | \psi_{n, \mathbf{k}} \rangle. \quad (3)$$

The velocity operator is expressed as the commutator of the Hamiltonian and the position operator $\hat{v}(\mathbf{r}) = i[H, \mathbf{r}] = \hat{p} + i[V^{NL}(\mathbf{r}, \mathbf{r}'), \mathbf{r}]$. For local potentials $V(\mathbf{r})$, the velocity operator \hat{v} is equivalent to the momentum operator \hat{p} and therefore in many cases the velocity matrix element $\langle \psi_{l, \mathbf{k}} | \hat{v} | \psi_{n, \mathbf{k}} \rangle$ is substituted by the momentum matrix element $\langle \psi_{l, \mathbf{k}} | \hat{p} | \psi_{n, \mathbf{k}} \rangle$ in the velocity gauge. However, for nonlocal potentials $V^{NL}(\mathbf{r}, \mathbf{r}')$ the position operator no longer commutes with the Hamiltonian and the velocity operator is no longer equivalent to the momentum operator. As a result, in order to calculate transition matrix elements from nonlocal potentials in the velocity gauge, the velocity operator has to be used or else a nonlocal correction to the momentum operator needs to be applied ($\hat{p} + i[V^{NL}(\mathbf{r}, \mathbf{r}'), \mathbf{r}]$). Otherwise the gauge invariance is violated [20, 21, 23]. In other words, for accurate optical matrix elements, the nonlocal potential must not be neglected. In the length gauge, nonlocal potentials are treated correctly automatically.

The nonlocality in the potential stems from the fact that the full-electron Hamiltonian is replaced by an approximate Hamiltonian in the independent-electron approximation with an effective potential that reintroduces electron-electron interactions in the Kohn-Sham equations [24, chap. 2]. There are several sources by which nonlocality may be introduced in the effective Hamiltonian [11, 21, 25]: an incomplete basis set, local field effects due to abrupt changes in the charge density (spatial inhomogeneity), nonlocal pseudopotentials and nonlocal exchange-correlation potentials or quasiparticle self-energies.

The importance of using the nonlocal correction in the velocity gauge has been widely discussed for nonlocal pseudopotentials [25–27]. It was shown that neglecting the nonlocal term in the velocity gauge leads to inaccurate matrix elements, especially for transitions that involve localized d-electrons [28]. Also, several works have investigated the nonlocal effects of the self-energy operator on transition matrix elements from many-body *GW* calculations [20, 21, 29]. At the DFT level, Rhim *et al.* [22] calculated optical matrix elements including non-local exchange with the screened-exchange LDA functional (sX-LDA). They showed that to obtain the correct band dispersion, opening the bandgap with a scissor operator is not enough and the full calculation of the matrix element effects is necessary. Further, Paier *et al.* [30] showed that including nonlocal exchange via hybrid functionals yields more accurate static and dynamic dielectric functions in comparison with semilocal functionals. In this work, we focus on the nonlocality introduced by a nonlocal hybrid exchange-correlation potential and its effect on the accuracy of calculated effective masses.

III. METHODS

A. Dataset

The data set contains 14 bulk and 4 monolayer materials with a total of 60 effective masses. Materials considered include sp-semiconductors and d-element semiconductors containing one transition metal. We include both three-dimensional and two-dimensional (layered) structures. The materials considered cover a wide range of effective masses. For the creation of the effective mass data set, we collected experimental effective mass data from the available literature. Most experimental data was taken from existing compilations in the Landolt-Börnstein database [31]. We also included several individual entries from the

literature for layered and monolayer 2D materials. Wherever multiple experimental values of one effective mass were available, we took the average for comparison with our computational data. For the compilation of the database, we had to exclude materials for which the experimentally reported effective masses differed widely, as this rendered comparison with computational results unprofitable.

B. DFT functionals

We computed the effective masses using three different exchange-correlation potentials that represent different levels of theory: The first level of theory used was the Perdew–Burke–Ernzerhof (PBE) [32] GGA exchange-correlation functional, which is semilocal in its treatment of exchange and correlation.

We also computed the effective masses with the Tran-Blaha modified Becke-Johnson potential (TB-mBJ) [13, 14] potential which corresponds to the second level of theory. The TB-mBJ potential

$$V_{x,\sigma}^{\text{mBJ}}(\mathbf{r}) = cV_{x,\sigma}^{\text{BR}}(\mathbf{r}) + (3c - 2)\frac{1}{\pi}\sqrt{\frac{5}{6}}\sqrt{\frac{t_{\sigma}(\mathbf{r})}{\rho_{\sigma}(\mathbf{r})}} \quad (4)$$

is also a semilocal approximation. It is based on the Becke-Roussel [33] potential $V_{x,\sigma}^{\text{BR}}(\mathbf{r})$ which models the Coulomb potential of the exchange hole. σ denotes the spin. Besides $V_{x,\sigma}^{\text{BR}}(\mathbf{r})$, the TB-mBJ potential includes a term proportional to $\sqrt{t_{\sigma}(\mathbf{r})/\rho_{\sigma}(\mathbf{r})}$, where t_{σ} is the kinetic energy density and ρ_{σ} is the electron density. This root term can be interpreted as a screening term [34]. While semilocal in its approach, TB-mBJ mimics nonlocal effects. The parameter c can be determined self-consistently. However, in our work we adjust the c parameter to reproduce the experimental band gap to eliminate an additional source of data scattering when comparing effective masses with experiment and hybrid functional calculations. The band gap was fitted with a maximum error of less than 2%.

On the third level of theory, we used the Heyd-Scuseria-Ernzerhof hybrid functional (HSE06) [35] to compute effective masses. In a hybrid functional, a percentage of nonlocal Hartree-Fock (HF) exchange is mixed with the local PBE exchange-correlation functional. For HSE, the exchange is divided into a short-range (SR) and a long-range (LR) contribution. Only for the short-range exchange, a part of the PBE exchange is replaced by the exact Hartree-Fock exchange. The long-range exchange is entirely taken from the PBE functional.

The HSE functional takes the form

$$E_{xc}^{\text{HSE}} = aE_x^{\text{HF,SR}}(\omega) + (1 - a)E_x^{\text{PBE,SR}}(\omega) + E_x^{\text{PBE,LR}}(\omega) + E_c^{\text{PBE}}, \quad (5)$$

where ω denotes the range separation between SR and LR. ω is set to 0.2 \AA^{-1} for the HSE06 functional. The parameter a specifies the percentage of SR Hartree-Fock exchange included. It is typically set to 0.25. In our work, we fitted a for each material to reproduce the experimental band gap with less than 2% error. This allowed us to directly compare HSE and TB-mBJ effective masses.

Because of the inclusion of a part of the exact nonlocal exchange, nonlocal exchange effects are considered explicitly. HF exchange is unscreened. The mixing of the nonlocal Hartree-Fock exchange with the local PBE exchange-correlation amounts to an effective screening of the nonlocal exchange by the local exchange-correlation [36], leading to a very good agreement with experiment for the electronic structure of semiconductors. Due to this artificial screening, the HSE approach can be seen as an approximation to the *GW* approach [11, chap. 9.2]. *GW* includes the dynamically screened exchange W in a physically correct way.

C. Computational details

Density functional calculations were performed with the Vienna *ab initio* simulation package [37, 38] (VASP), which uses projector-augmented waves [39] as basis set, implemented by Kresse and Joubert [40]. The plane wave cutoffs were taken from the values recommended in the pseudopotentials distributed with VASP. The number of valence and semicore electrons included for each element was chosen according to the values recommended by the materials project database [41]. For molybdenum and tungsten we included additional semi-core states (14 valence and semi-core electrons in total). The Brillouin zone was sampled with k grids ranging between $6 \times 6 \times 6$ and $8 \times 8 \times 8$ for the bulk materials, depending on where the band extrema were located in the Brillouin zone. For monolayers, k grids of $6 \times 6 \times 1$ were used.

Experimental lattice parameters were used for all bulk systems, allowing only atomic positions to relax using the PBE functional with a force convergence criterium of 0.001 eV/\AA . Experimental structure data were obtained from Wyckoff [42] unless otherwise specified in

Table I. The monolayers were obtained by theoretical exfoliation from the corresponding bulk material. To avoid interactions between periodic images of a monolayer, more than 25 Å of vacuum were included in the out-of-plane direction. Subsequently, the monolayers were fully relaxed on the PBE level.

All systems were treated as non-magnetic. Spin-orbit coupling was included in all calculations. Additional system-dependent calculation parameters are recorded in Table S1 of the supplementary information. Table S1 lists the experimental bandgaps (Refs. [43–49]) that were used to fit the HSE and TB-mBJ band gaps, the fitting parameters and the number of bands included in the optical calculations. We performed optical calculations in VASP to compute the transition matrix elements. In VASP, the longitudinal gauge (see Eq. (2)) is implemented for the calculation of the transition matrix elements [27]. In this gauge, nonlocal potentials are evaluated correctly.

Effective masses were calculated with the `mstar` code [17] which uses a perturbation theory approach based on Eq. (1) and its extension for degenerate states. The perturbation approach includes a sum over all bands and therefore many empty bands have to be included for accurate effective mass calculations. This is especially true for heavy effective masses and band edges that interact with high-energy orbitals. For the optical calculations, we included empty bands of up to 7 Ry (96 eV) above the Fermi level to ensure an accurate calculation of the effective mass. 7 Ry suffices for most materials but not for all, as we will discuss later. In contrast to Fourier expansion methods for calculating effective masses (as implemented in the `BoltzTraP` code [50]), the perturbation approach does not require a dense k grid to accurately capture light effective masses.

D. Statistics

The computational effective masses were compared with the experimental values. For the statistical analysis, we determined the mean error (ME), mean absolute error (MAE), mean relative error (MRE) and the mean absolute relative error (MARE). The standard deviation of the error (STDE) and the relative error (STDRE) were also calculated. Only materials for which data for all functionals was collected were included in the statistical analysis. Errors with a z-score of more than 3.5 were treated as outliers.

IV. RESULTS AND DISCUSSION

Table I shows the results for 60 effective masses of 14 bulk and 4 monolayer materials obtained with different exchange-correlation potentials. Figure 1 shows the data of Table I graphically. To keep with the convention, the sign of the valence band effective masses is inverted, that is, a valence band curving downwards yields a positive effective mass. Negative values denote an upwards-bent valence band or a downwards-bent conduction band.

First, we need to ensure that our method is reliable. We compare the perturbation theory results at the PBE level with band curvature fits for which the band of interest was fitted in an energy window of 25 meV (the thermal energy at room temperature) with a fourth-order polynomial and extracted the second order coefficient. For GaAs we compared m_n , $m_{p,hh}$, $m_{p,lh}$ and $m_{p,so}$ and found that perturbation theory results agreed within an error of 1% with the band curvature fit. For Si, $m_{p,hh}$, $m_{p,lh}$ and $m_{p,so}$ agreed within 2.5% error. For 1L MoS₂ at the K point the band curvature yields $m_p(K) = 0.523 m_0$ which is 15% smaller than the perturbation theory result. The conduction band effective mass from the band curvature is $m_n(K) = 0.431 m_0$ which is 7% larger than the perturbation theory result. This is due to challenges with representing d-states using perturbation theory as discussed further below.

Previous effective mass calculations at the PBE level agree well with our results. For example, for the conduction band effective masses of Silicon, our results agree well with the ones obtained by Zhong *et al.* [51] and Yu *et al.* [52] (in brackets), respectively: $m_{n,\parallel} = 0.943$ (0.950; 0.95) and $m_{n,\perp} = 0.193$ (0.197; 0.19) (all effective masses in units of m_0). For GaAs, our values agree well with the results reported by Kim *et al.* [8] (in brackets): $m_{p,so} = 0.107$ (0.108), $m_{p,lh} = 0.034$ (0.036), $m_{p,hh} = 0.324$ (0.320) and $m_n = 0.028$ (0.030). For monolayer MoS₂ our data at the K point show satisfactory agreement with the results of Wang *et al.* [53], Kormányos *et al.* [54] and Wang *et al.* [55] (in brackets), respectively: $m_p(K) = 0.603$ (0.59; 0.56; 0.54), $m_n(K) = 0.402$ (0.5; 0.47; 0.47). Our results for monolayer MoS₂ are discussed in more detail below. Overall, our perturbation theory results are accurate with respect to band curvature fits and agree very well with previously published data, especially for sp-semiconductors.

We begin with the discussion of the summary statistics. Table II shows the summary statistics for the `mstar60` dataset, listing the following quantities: ME, MAE, MRE, MARE, STDE, and STDRE. We included only materials for which effective masses were obtained

with all three functionals. In spite of being very effective for most solids, the TB-mBJ potential (as well as its local version [56] designed for materials with vacuum) was unable to open the band gap beyond PBE for monolayers of MoS₂, MoSe₂, WS₂, and WSe₂ as also noted by Patra *et al.* [57] and further explained by Tran *et al.* [58]. As a result, we did not calculate masses in monolayers with TB-mBJ and excluded them from the statistical analysis. Black phosphorus was also excluded because representative effective masses could not be obtained at the PBE level. At the PBE level, the conduction band of black phosphorus is lower in energy than the valence band, leading to a metallic ground state with band inversion and band mixing around the band edges. This causes effective masses of inverted sign and magnitude in two directions. A proper band order is restored at a higher level of theory (HSE, TB-mBJ). Furthermore, the following effective masses were excluded from the statistical analysis as outliers with a z-score above 3.5: GaAs $m_{n,\parallel}$ (X6), CdS $m_{p,\parallel}$ (Γ , A exciton), and BN m_p (\bar{K}). The outliers are marked with † in Table I. In total, 42 effective masses of 13 materials were included in the statistical analysis.

Effective masses calculated with the PBE functional show the largest errors, with a mean absolute relative error of 38% and a mean relative error of -27%. The negative values of mean error and mean relative error suggest that effective masses are in many cases underestimated. However, the scattering of the error is large as indicated by the standard deviation of the relative error of 40%.

Effective masses calculated with the HSE functional fitted for the band gap show the best agreement with experiment throughout with a mean absolute relative error of 10% and a mean relative error of -4.7%. The errors are much smaller than the absolute errors for HSE which shows that there is no clear trend for over- or underestimation of the effective mass using HSE.

Turning to results obtained with the TB-mBJ functional fitted for the band gap, the mean absolute relative error is 21%, which is about twice that of HSE but less than the error of PBE. The mean relative error of 16% is positive. So, in contrast to effective masses calculated with the PBE functional, effective masses obtained with TB-mBJ are very often overestimated with respect to experiment.

The main conclusion of the benchmarking of the PBE, HSE (gap fit) and TB-mBJ (gap fit) exchange-correlation potentials is that HSE gives by far the best agreement with experimental effective masses. On the other hand, PBE often yields lighter effective masses, while

TB-mBJ generally overestimates them. These trends are in agreement with the results of Kim *et al.* [8].

Our objective is to comprehend with greater clarity the properties of hybrid functionals that make HSE so successful in reproducing experimental effective masses. As stated earlier, the main difference of the hybrid functionals with respect to semilocal functionals is the addition of a nonlocal component via the introduction of a fraction of HF exchange. Effective masses are influenced by the nonlocal component in two ways: Firstly, by adding nonlocal exchange, the band gap opens up, which increases the effective mass. Secondly, nonlocal effects influence the optical transition matrix elements p_{ln} . The opening of the band gap can be reproduced with the TB-mBJ potential, but the errors in the effective masses are still much higher than with HSE.

We now want to probe the role of the nonlocal exchange potential V_x^{NL} for the calculation of the matrix element. To that end it is instructive to switch off the nonlocal exchange contributions in the matrix element. We achieve this by switching to the PBE potential when calculating the matrix elements while using HSE wavefunctions (see supplementary information for the detailed workflow). As a result, HSE eigenfunctions and band gaps are conserved and only the matrix element is calculated without nonlocal exchange effects. This allows us to decouple the band gap increase and the matrix element change that are both caused by the nonlocal exchange.

Switching off the nonlocal exchange contributions to the matrix elements leads to a systematic overestimation of the effective masses (see Fig. 1 and Table I), with only a few exceptions. This is a consequence of the absolute matrix element being *smaller* when calculated without the nonlocal exchange potential.

Let us consider the example of the conduction band effective mass m_n of GaAs at Γ to discuss the nonlocal exchange contribution to the effective mass in more detail. Figure 2 shows the effective mass of the conduction band of GaAs at Γ versus the band gap for different settings of the exchange-correlation functional. For this graph, the electron effective mass was approximated as:

$$\frac{m_0}{m_n^*} \approx 1 + \frac{2}{m_0} \sum_{\mathbf{v}} \frac{|p_{c\mathbf{v}}|^2}{E_c - E_{\mathbf{v}}}, \quad (6)$$

where the ‘c’ and ‘v’ indices stand for the conduction band and valence bands, respectively.

In GaAs, the effective mass of the conduction band at the Γ point is isotropic and therefore the matrix element contribution can be expressed as $2|p_{cv}|^2$. In the sum, we included the heavy-hole, light-hole and split-off bands as valence bands. As not all bands are included in the sum, this is an approximation. The matrix elements are calculated in the length gauge using VASP.

In Fig. 2 we observe a linear relationship between the effective mass and the band gap for all XC functionals that do not include nonlocal exchange. This is a consequence of the fact that $\sum |p_{cv}|^2$ changes very little, and thus the change in effective mass depends only on the change of the band gap. Effective masses obtained from hybrid functionals considering nonlocal exchange deviate from that linear relationship. Only upon including nonlocal exchange both the experimental band gap and experimental effective mass can be reproduced correctly in the calculation. Figure 2 thus shows the importance of including the nonlocal exchange on the HSE level for calculating accurate matrix elements and thus accurate effective masses when employing perturbation theory. The same matrix elements are also used in the calculation of optical properties, which explains the superior accuracy of HSE for the high-frequency dielectric constant of semiconductors and small-gap insulators [30].

The deviation from the linear relationship indicates that $\sum |p_{cv}|^2$ changes when the nonlocal exchange potential V_x^{NL} is included in the calculation of the matrix element. Thus, the matrix element is the key parameter we need to consider if we want to explain the superior accuracy of HSE effective masses, especially compared to TB-mBJ results.

Figure 3 shows the sum of the squared matrix elements $\sum |p_{cv}|^2$ that enter into Eq. (6) versus the band gap for different settings of the exchange-correlation functional for the conduction band effective mass of GaAs at Γ . Again, the sum displayed on the vertical axis includes contributions from the transitions between the conduction band and the heavy-hole, light-hole and split-off valence bands. $\sum |p_{cv}|^2$ is around 0.6 atomic units for all XC functionals that do not include nonlocal effects, irrespective of the band gap. We included data obtained with Wien2k [59, 60] at the PBE level for comparison. We also calculated the matrix elements from the semilocal SCAN [61] functional, which gives the same matrix element as TB-mBJ and PBE in spite of the band gap being intermediate between PBE and TB-mBJ. When the nonlocal exchange potential V_x^{NL} is considered in the calculation of the matrix element, $\sum |p_{cv}|^2$ increases with increasing HF proportion and increasing the band gap. The change of the sum $\sum |p_{cv}|^2$ is the key that leads to the deviation of full HSE

results from the linear pattern of Fig. 2. Interestingly, the increase of $\sum |p_{cv}|^2$ is strictly proportional to the increase of the HF percentage included in the functional.

This observation of a larger $\sum |p_{cv}|^2$ for hybrid functionals aligns with our physical intuition according to which nonlocal exchange makes the interaction between two states more efficient and thus increases the matrix element. This can be seen when considering the origin of exchange and correlation in the density functional theory: We first make the independent electron approximation, assuming that electrons do not interact at all. Afterwards, we introduce their interaction via a mean-field repulsion, the Hartree term. However, that mean-field interaction overestimates the repulsion an electron actually feels. This overestimated repulsion is then compensated by the reintroduction of correlation and exchange effects. Therefore, we need to include these corrective effects in order to lower the energy of our system and adequately predict electron-electron interaction. With semilocal functionals like LDA/GGA, we correct only for a local part of the inherently nonlocal exchange. This means that we are still overestimating the repulsion between electrons. If we now include a part of the nonlocal exact exchange, we lower the repulsion. The electron is less constrained to interact with other electronic states leading to more dispersive bands. As a result, the matrix element increases. In other words, the electronic states can interact more efficiently due to the nonlocal term in the Hamiltonian. With increasing nonlocal HF exchange included in the HSE functional, the corresponding matrix element increases in magnitude as seen in Fig. 3.

Having analyzed the effect of the nonlocal exchange on the transition matrix element, we can add some comments on the general trends observed for effective masses in Fig. 1 and the summary statistics of Table II. Starting with TB-mBJ calculated effective masses, the clear trend for overestimation comes from the too-small absolute matrix elements. This is the same for HSE effective masses for which V_x^{NL} was neglected in the calculation of the matrix element. On the other hand, for PBE calculated effective masses, no clear trend is apparent. For some PBE effective masses, e.g. Si $m_{n,\perp}$ and $m_{n,\parallel}$, the agreement with experiment is surprisingly good. This is because the PBE band gap is not fitted to the experimental band gap. As a result, errors in the effective mass due to an underestimated band gap and due to the underestimated matrix element partially cancel out. This error cancellation is not systematic as seen by the high standard deviation of the relative error of 41%. Therefore, no clear trend for the error of PBE effective masses can be found.

We now turn our attention to the monolayer effective mass values recorded in Table I. For some effective masses at Γ , reliable PBE-derived effective masses could not be obtained with perturbation theory as the result differed by more than 30% from the band curvature fit. For effective masses at the K point, the errors with respect to the band curvature were in the range of 5 – 16% which is significantly larger than for sp-semiconductors. The variations of the perturbation theory results with respect to the band curvature obtained with PBE can be explained with the limits of perturbation theory in connection with DFT pseudopotentials. All monolayers considered in our study are transition metal dichalcogenides for which the band edges are composed mainly of the d-orbitals of the transition metal. When it comes to the prediction of d-states, it is difficult to converge the perturbation sum. According to the optical selection rule $\Delta l = \pm 1$, l being the orbital quantum number, d-states couple with p-states and f-states. Therefore, many high-energy empty bands have to be included that describe the f-states in order to correctly converge the perturbation sum for d-states. In other words, the convergence of the sum with respect to the number of empty bands needs to be carefully tested. This is true not only for effective masses but for all electronic structure methods that are based on perturbation theory, e.g., *GW*. We included 800 bands for the calculation of the effective masses in the monolayers, which corresponds to ca. 5 – 6 Ry above the Fermi level.

When we increase the number of empty bands, the predicted effective mass is slowly corrected towards the value obtained from parabolic fitting of the band edge (see Table S2 of the supplementary information). However, for the example of 1L MoS₂ even with about 2400 bands (ca. 12 Ry above the Fermi level), the error is still high. We also notice that the effective mass predicted depends on the pseudopotential employed. For 1L MoS₂, the error is greater for the Mo_{pv} pseudopotential than for the Mo_{sv} potential and the Mo_{sv}-*GW* potential which has the lowest error. This is because in the *GW* pseudopotentials the high-energy electron scattering is more accurate, rendering the *GW* pseudopotentials better suited for calculations that include coupling to high-energy states [39, 62]. In bulk MoS₂ and WS₂, we see similar errors of PT results with respect to the band curvature, though reduced in magnitude (Table S2 of the supplementary information). We conclude that the prediction of the effective mass of d-states is challenging in two ways: Firstly, a high number of empty bands has to be included and secondly, even when they are included, the physical limits of the pseudopotentials are reached.

The sum over many empty states in the perturbative expansion can elegantly be overcome with the Sternheimer approach [63] as shown in the context of quasiparticle *GW* calculations [64] or effective masses [65] which do not require the computation of unoccupied electronic states. Alternatively, it is possible to address this issue by including high-energy local orbitals (HELOs) to augment the basis set. This feature available in the Wien2k code was shown to improve the magnetic shielding for solid state nuclear magnetic resonance [66], effective masses derived from the perturbative expansion [17] and the *GW* band gap convergence [67]. With six high-energy local orbitals included, the effective mass of 1L MoS₂ predicted with perturbation theory is in good agreement with the band curvature fit (Table S2 of the supplementary information; see supplementary information for the detailed workflow of Wien2k calculations with HELOs).

The limits observed for d-states at the example of PBE hold also for HSE calculations. Here, a further aspect is noteworthy. To fit the transport band gap of the monolayer materials we have to include a large proportion of HF exchange in the hybrid functional (see Table S1 in the supplementary information). Relative to the HF percentage for the parent bulk structure we had to include nearly three times the HF proportion for 1L MoS₂ and about four times the HF proportion for 1L WS₂ to obtain the right band gap. Considering that the same chemical elements are used, this seems surprising. It points to the limit of the parameter fitting procedure to obtain the experimental transport band gap for monolayer 2D materials. The large percentage of HF included in the functional may lead to an unphysical increase of the matrix element, which may be the reason why many effective masses are smaller than the experimental value (see Table I).

Turning away from technical aspects, we now look at the experimental effective masses for the transition metal dichalcogenide monolayers recorded in Table I. We observe that the bulk MoS₂ hole effective mass at Γ is much lighter than the 1L MoS₂ effective mass. To explain this effective mass renormalization, we can consider two factors (drawing on Eq. (1)): the band gap change and the change of the matrix element. The band gap at Γ opens up from 2.08 eV in the bulk to 2.84 eV in the monolayer MoS₂ at the PBE level. Looking into the matrix elements, we observe that the coupling of the lower-lying conduction bands with the valence band at Γ contributes significantly to the band dispersion. Thus, an increase of the band gap affects the strength of the contribution of these interactions to the band curvature. However, the band gap renormalization accounts for only less than half of the effective mass

renormalization. This means that also the matrix elements themselves change: In 1L MoS₂ the sum of these matrix elements is only about half of that in bulk MoS₂. In other words, the oscillator strength between the valence band (VB) at Γ and the lower-lying conduction bands is much weaker in the monolayer than in the bulk. As a result, the band dispersion of the VB at Γ is flatter in 1L MoS₂ and the effective mass is larger.

The layer-dependent effective mass of holes at the Γ point in MoS₂ is an example that we have to consider the change of the optical matrix element when trying to explain effective mass renormalization effects. This example shows that in order to develop a physical intuition for the renormalization of effective masses, both the band gap and the matrix element renormalization have to be considered together.

V. CONCLUSION

In summary, we benchmarked the performance of three exchange-correlation potentials for the calculation of effective masses. For benchmarking we introduced the `mstar60` dataset which contains 18 semiconductors with a wide range of electronic properties and effective masses. Our calculations show that the hybrid HSE06 functional (fitted to the experimental band gap) yields by far the most accurate effective masses with respect to experiment, followed by the TB-mBJ functional (fitted to the experimental band gap). We reveal that the nonlocal exchange in HSE06 enlarges the transition matrix elements which proves to be the key to the superior accuracy in the calculation of effective masses. The omission of the commutator between the nonlocal XC potentials and position when calculating optical matrix elements in HSE leads to serious errors (about 30% underestimated p_{cv}^2 matrix elements in GaAs). For the semilocal PBE functional, the errors introduced by the band gap and the transition matrix elements partially cancel out for the calculation of effective masses. We discuss the limits of the perturbation approach to the calculation of effective masses for d-states and possible solutions. Finally, we show at the example of transition metal dichalcogenide bulk and monolayer materials that changes in the matrix elements are important in understanding the layer-dependent effective mass renormalization. In this, our analysis goes beyond the standard discussion that focusses on the interband energy difference. Our results show that changes in the matrix elements may not be ignored in the discussion of effective mass renormalization effects.

ACKNOWLEDGMENTS

The authors are thankful to Peter Blaha and Fabien Tran (TU Vienna) for the insightful discussion about the performance of a (local) TB-mBJ potential for transition metal dichalcogenides. The authors acknowledge funding provided by the Natural Sciences and Engineering Research Council of Canada under the Discovery Grant Programs RGPIN-2020-04788. Calculations were performed using the Compute Canada infrastructure supported by the Canada Foundation for Innovation under John R. Evans Leaders Fund.

-
- [1] G. Hautier, A. Miglio, D. Waroquiers, G.-M. Rignanese, and X. Gonze, How Does Chemistry Influence Electron Effective Mass in Oxides? A High-Throughput Computational Analysis, *Chem. Mater.* **26**, 5447 (2014).
- [2] S. Curtarolo, W. Setyawan, S. Wang, J. Xue, K. Yang, R. H. Taylor, L. J. Nelson, G. L. W. Hart, S. Sanvito, M. Buongiorno-Nardelli, N. Mingo, and O. Levy, AFLOWLIB.ORG: A distributed materials properties repository from high-throughput ab initio calculations, *Comput. Mater. Sci.* **58**, 227 (2012).
- [3] G. Hautier, A. Miglio, G. Ceder, G.-M. Rignanese, and X. Gonze, Identification and design principles of low hole effective mass p-type transparent conducting oxides, *Nat. Commun.* **4**, 2292 (2013).
- [4] E. Tsymbalov, Z. Shi, M. Dao, S. Suresh, J. Li, and A. Shapeev, Machine learning for deep elastic strain engineering of semiconductor electronic band structure and effective mass, *npj Comput. Mater.* **7**, 1 (2021).
- [5] S. Hastrup, M. Strange, M. Pandey, T. Deilmann, P. S. Schmidt, N. F. Hinsche, M. N. Gjerding, D. Torelli, P. M. Larsen, A. C. Riis-Jensen, *et al.*, The computational 2d materials database: high-throughput modeling and discovery of atomically thin crystals, *2D Materials* **5**, 042002 (2018).
- [6] N. W. Ashcroft, A. W. i. W. Ashcroft, and N. D. Mermin, *Solid State Physics* (Holt, Rinehart and Winston, 1976).
- [7] P. Y. Yu and M. Cardona, *Fundamentals of semiconductors: physics and materials properties*, 4th ed., Graduate texts in physics (Springer, Berlin, New York, 2010).
- [8] Y.-S. Kim, M. Marsman, G. Kresse, F. Tran, and P. Blaha, Towards efficient band structure and effective mass calculations for III-V direct band-gap semiconductors, *Phys. Rev. B* **82**, 205212 (2010).
- [9] W. G. Zeier, A. Zevalkink, Z. M. Gibbs, G. Hautier, M. G. Kanatzidis, and G. J. Snyder, Thinking Like a Chemist: Intuition in Thermoelectric Materials, *Angewandte Chemie International Edition* **55**, 6826 (2016).
- [10] W. Kohn and L. J. Sham, Self-consistent equations including exchange and correlation effects, *Phys. Rev.* **140**, A1133 (1965).

- [11] F. Bechstedt, *Many-Body Approach to Electronic Excitations*, Springer Series in Solid-State Sciences, Vol. 181 (Springer Berlin Heidelberg, Berlin, Heidelberg, 2015).
- [12] W. Li and F. Giustino, Many-body renormalization of the electron effective mass of InSe, *Phys. Rev. B* **101**, 035201 (2020).
- [13] A. D. Becke and E. R. Johnson, A simple effective potential for exchange, *J. Chem. Phys.* **124**, 221101 (2006).
- [14] F. Tran and P. Blaha, Accurate Band Gaps of Semiconductors and Insulators with a Semilocal Exchange-Correlation Potential, *Phys. Rev. Lett.* **102**, 226401 (2009).
- [15] H. Dixit, R. Saniz, S. Cottenier, D. Lamoen, and B. Partoens, Electronic structure of transparent oxides with the Tran–Blaha modified Becke–Johnson potential, *J. Phys.: Condens. Matter* **24**, 205503 (2012).
- [16] R. B. Araujo, J. S. de Almeida, and A. Ferreira da Silva, Electronic properties of III-nitride semiconductors: A first-principles investigation using the Tran-Blaha modified Becke-Johnson potential, *J. Appl. Phys.* **114**, 183702 (2013).
- [17] O. Rubel, F. Tran, X. Rocquefelte, and P. Blaha, Perturbation approach to ab initio effective mass calculations, *Comput. Phys. Commun.* **261**, 107648 (2021).
- [18] G. F. Bassani and G. Pastori Parravicini, *Electronic states and optical transitions in solids*, 1st ed., International series of monographs in the science of the solid state No. v. 8 (Pergamon Press, Oxford ; New York, 1975).
- [19] D. Marti, M.-A. Dupertuis, and B. Deveaud, General theory for the interference of two-photon and one-photon processes in semiconductor heterostructures, *Ann. Phys.* **316**, 234 (2005).
- [20] R. Del Sole and R. Girlanda, Optical properties of semiconductors within the independent-quasiparticle approximation, *Phys. Rev. B* **48**, 11789 (1993).
- [21] B. Adolph, V. I. Gavrilenko, K. Tenelsen, F. Bechstedt, and R. Del Sole, Nonlocality and many-body effects in the optical properties of semiconductors, *Phys. Rev. B* **53**, 9797 (1996).
- [22] S. H. Rhim, M. Kim, A. J. Freeman, and R. Asahi, Fully first-principles screened-exchange LDA calculations of excited states and optical properties of III-V semiconductors, *Phys. Rev. B* **71**, 045202 (2005).
- [23] A. F. Starace, Length and Velocity Formulas in Approximate Oscillator-Strength Calculations, *Phys. Rev. A* **3**, 1242 (1971).

- [24] F. Giustino, *Materials Modelling using Density Functional Theory Properties and Predictions* (Oxford University Press, 2014).
- [25] C. J. Pickard and M. C. Payne, Second-order $k \cdot p$ perturbation theory with Vanderbilt pseudopotentials and plane waves, *Phys. Rev. B* **62**, 4383 (2000).
- [26] S. Ismail-Beigi, E. K. Chang, and S. G. Louie, Coupling of Nonlocal Potentials to Electromagnetic Fields, *Phys. Rev. Lett.* **87**, 087402 (2001).
- [27] M. Gajdoš, K. Hummer, G. Kresse, J. Furthmüller, and F. Bechstedt, Linear optical properties in the projector-augmented wave methodology, *Phys. Rev. B* **73**, 045112 (2006).
- [28] A. J. Read and R. J. Needs, Calculation of optical matrix elements with nonlocal pseudopotentials, *Phys. Rev. B* **44**, 13071 (1991).
- [29] Z. H. Levine and D. C. Allan, Optical second-harmonic generation in III-V semiconductors: Detailed formulation and computational results, *Phys. Rev. B* **44**, 12781 (1991).
- [30] J. Paier, M. Marsman, and G. Kresse, Dielectric properties and excitons for extended systems from hybrid functionals, *Physical Review B* **78**, 121201 (2008).
- [31] Landolt-Börnstein — group III condensed matter.
- [32] J. P. Perdew, K. Burke, and M. Ernzerhof, Generalized Gradient Approximation Made Simple, *Phys. Rev. Lett.* **77**, 3865 (1996).
- [33] A. D. Becke and M. R. Roussel, Exchange holes in inhomogeneous systems: A coordinate-space model, *Phys. Rev. A* **39**, 3761 (1989).
- [34] D. Koller, F. Tran, and P. Blaha, Merits and limits of the modified Becke-Johnson exchange potential, *Phys. Rev. B* **83**, 195134 (2011).
- [35] A. V. Krukau, O. A. Vydrov, A. F. Izmaylov, and G. E. Scuseria, Influence of the exchange screening parameter on the performance of screened hybrid functionals, *J. Chem. Phys.* **125**, 224106 (2006).
- [36] A. D. Becke, Perspective: Fifty years of density-functional theory in chemical physics, *J. Chem. Phys.* **140**, 18A301 (2014).
- [37] G. Kresse and J. Furthmüller, Efficient iterative schemes for ab initio total-energy calculations using a plane-wave basis set, *Phys. Rev. B* **54**, 11169 (1996).
- [38] G. Kresse and J. Furthmüller, Efficiency of ab-initio total energy calculations for metals and semiconductors using a plane-wave basis set, *Comput. Mater. Sci.* **6**, 15 (1996).
- [39] P. E. Blöchl, Projector augmented-wave method, *Phys. Rev. B* **50**, 17953 (1994).

- [40] G. Kresse and D. Joubert, From ultrasoft pseudopotentials to the projector augmented-wave method, *Phys. Rev. B* **59**, 1758 (1999).
- [41] A. Jain, S. P. Ong, G. Hautier, W. Chen, W. D. Richards, S. Dacek, S. Cholia, D. Gunter, D. Skinner, G. Ceder, and K. A. Persson, Commentary: The Materials Project: A materials genome approach to accelerating materials innovation, *APL Mater.* **1**, 011002 (2013).
- [42] R. W. G. Wyckoff, *Crystal Structures, Vol. 1*, 2nd ed. (Wiley, 1963).
- [43] O. Madelung, *Semiconductors: Data Handbook* (Springer Science & Business Media, 2004).
- [44] K. K. Kam and B. A. Parkinson, Detailed photocurrent spectroscopy of the semiconducting group VIB transition metal dichalcogenides, *The Journal of Physical Chemistry* **86**, 463 (1982).
- [45] D. A. Evans, A. G. McGlynn, B. M. Towison, M. Gunn, D. Jones, T. E. Jenkins, R. Winter, and N. R. J. Poolton, Determination of the optical band-gap energy of cubic and hexagonal boron nitride using luminescence excitation spectroscopy, *Journal of Physics: Condensed Matter* **20**, 075233 (2008), publisher: IOP Publishing.
- [46] Y. L. Huang, Y. Chen, W. Zhang, S. Y. Quek, C.-H. Chen, L.-J. Li, W.-T. Hsu, W.-H. Chang, Y. J. Zheng, W. Chen, and A. T. S. Wee, Bandgap tunability at single-layer molybdenum disulphide grain boundaries, *Nature Communications* **6**, 6298 (2015).
- [47] M. M. Ugeda, A. J. Bradley, S.-F. Shi, F. H. da Jornada, Y. Zhang, D. Y. Qiu, W. Ruan, S.-K. Mo, Z. Hussain, Z.-X. Shen, F. Wang, S. G. Louie, and M. F. Crommie, Giant bandgap renormalization and excitonic effects in a monolayer transition metal dichalcogenide semiconductor, *Nature Materials* **13**, 1091 (2014).
- [48] B. Zhu, X. Chen, and X. Cui, Exciton Binding Energy of Monolayer WS₂, *Scientific Reports* **5**, 10.1038/srep09218 (2015).
- [49] C. Zhang, Y. Chen, A. Johnson, M.-Y. Li, L.-J. Li, P. C. Mende, R. M. Feenstra, and C.-K. Shih, Probing Critical Point Energies of Transition Metal Dichalcogenides: Surprising Indirect Gap of Single Layer WSe₂, *Nano Letters* **15**, 6494 (2015), publisher: American Chemical Society.
- [50] G. K. H. Madsen and D. J. Singh, BoltzTraP. A code for calculating band-structure dependent quantities, *Comput. Phys. Commun.* **175**, 67 (2006).
- [51] S. Zhong, M. Wu, and X. Lei, First-principle calculations of effective mass of silicon crystal with vacancy defects, *Mater. Sci.-Poland* **34**, 916 (2016).

- [52] D. Yu, Y. Zhang, and F. Liu, First-principles study of electronic properties of biaxially strained silicon: Effects on charge carrier mobility, *Phys. Rev. B* **78**, 245204 (2008).
- [53] L. Wang, A. Kutana, and B. I. Yakobson, Many-body and spin-orbit effects on direct-indirect band gap transition of strained monolayer MoS₂ and WS₂, *Ann. Phys.* **526**, L7 (2014).
- [54] A. Kormányos, G. Burkard, M. Gmitra, J. Fabian, V. Zólyomi, N. D. Drummond, and V. Fal'ko, $k \cdot p$ theory for two-dimensional transition metal dichalcogenide semiconductors, *2D Mater.* **2**, 022001 (2015).
- [55] V. Wang, N. Xu, J.-C. Liu, G. Tang, and W.-T. Geng, Vaspkit: a user-friendly interface facilitating high-throughput computing and analysis using vasp code, *Comput. Phys. Commun.* , 108033 (2021).
- [56] T. Rauch, M. A. Marques, and S. Botti, Local modified becke-johnson exchange-correlation potential for interfaces, surfaces, and two-dimensional materials, *J. Chem. Theory Comput.* **16**, 2654 (2020).
- [57] A. Patra, S. Jana, P. Samal, F. Tran, L. Kalantari, J. Doumont, and P. Blaha, Efficient band structure calculation of two-dimensional materials from semilocal density functionals, *J. Phys. Chem. C* (2021).
- [58] F. Tran, J. Doumont, L. Kalantari, P. Blaha, T. Rauch, P. Borlido, S. Botti, M. A. L. Marques, A. Patra, S. Jana, and P. Samal, Bandgap of two-dimensional materials: Thorough assessment of modern exchange–correlation functionals, *The Journal of Chemical Physics* **155**, 104103 (2021).
- [59] P. Blaha, K. Schwarz, G. K. H. Madsen, D. Kvasnicka, J. Luitz, R. Laskowsk, F. Tran, L. Marks, and L. Marks, *WIEN2k: An Augmented Plane Wave Plus Local Orbitals Program for Calculating Crystal Properties* (Techn. Universitat, 2019).
- [60] P. Blaha, K. Schwarz, F. Tran, R. Laskowski, G. K. Madsen, and L. D. Marks, Wien2k: An apw+ lo program for calculating the properties of solids, *J. Chem. Phys.* **152**, 074101 (2020).
- [61] J. Sun, A. Ruzsinszky, and J. Perdew, Strongly Constrained and Appropriately Normed Semilocal Density Functional, *Phys. Rev. Lett.* **115**, 036402 (2015).
- [62] T. R. Mattsson, S. Root, A. E. Mattsson, L. Shulenburg, R. J. Magyar, and D. G. Flicker, Validating density-functional theory simulations at high energy-density conditions with liquid krypton shock experiments to 850 GPa on Sandia’s Z machine, *Phys. Rev. B* **90**, 184105 (2014).

- [63] R. Sternheimer, On nuclear quadrupole moments, *Physical Review* **84**, 244 (1951).
- [64] F. Giustino, M. L. Cohen, and S. G. Louie, Gw method with the self-consistent sternheimer equation, *Physical Review B* **81**, 115105 (2010).
- [65] J. Laflamme Janssen, Y. Gillet, S. Poncé, A. Martin, M. Torrent, and X. Gonze, Precise effective masses from density functional perturbation theory, *Phys. Rev. B* **93**, 205147 (2016).
- [66] R. Laskowski and P. Blaha, Calculating nmr chemical shifts using the augmented plane-wave method, *Physical Review B* **89**, 014402 (2014).
- [67] X. Ren, F. Merz, H. Jiang, Y. Yao, M. Rampp, H. Lederer, V. Blum, and M. Scheffler, All-electron periodic G_0W_0 implementation with numerical atomic orbital basis functions: Algorithm and benchmarks, *Physical Review Materials* **5**, 013807 (2021).
- [68] R. Dexter and B. Lax, Effective masses of holes in silicon, *Physical Review* **96**, 223 (1954).
- [69] P. Rochon and E. Fortin, Photovoltaic effect and interband magneto-optical transitions in inp, *Physical Review B* **12**, 5803 (1975).
- [70] Y. G. Andreev and T. Lundström, On the influence of nitrogen pressure on the ordering of hexagonal boron nitride, *J. Alloys Compd.* **216**, L5 (1994).
- [71] H. Henck, D. Pierucci, G. Fugallo, J. Avila, G. Cassabois, Y. J. Dappe, M. G. Silly, C. Chen, B. Gil, M. Gatti, F. Sottile, F. Sirotti, M. C. Asensio, and A. Ouerghi, Direct observation of the band structure in bulk hexagonal boron nitride, *Phys. Rev. B* **95**, 085410 (2017).
- [72] S.-i. Narita, S.-i. Terada, S. Mori, K. Muro, Y. Akahama, and S. Endo, Far-Infrared Cyclotron Resonance Absorptions in Black Phosphorus Single Crystals, *J. Phys. Soc. Jpn.* **52**, 3544 (1983).
- [73] P. B. James and M. T. Lavik, The crystal structure of $MoSe_2$, *Acta Crystallogr.* **16**, 1183 (1963).
- [74] W. Jin, P.-C. Yeh, N. Zaki, D. Zhang, J. T. Sadowski, A. Al-Mahboob, A. M. van der Zande, D. A. Chenet, J. I. Dadap, I. P. Herman, P. Sutter, J. Hone, and R. M. Osgood, Direct measurement of the thickness-dependent electronic band structure of MoS_2 using angle-resolved photoemission spectroscopy, *Phys. Rev. Lett.* **111**, 106801 (2013).
- [75] I. Tanabe, M. Gomez, W. C. Coley, D. Le, E. M. Echeverria, G. Stecklein, V. Kandyba, S. K. Balijepalli, V. Klee, A. E. Nguyen, E. Preciado, I.-H. Lu, S. Bobek, D. Barroso, D. Martinez-Ta, A. Barinov, T. S. Rahman, P. A. Dowben, P. A. Crowell, and L. Bartels, Band structure characterization of WS_2 grown by chemical vapor deposition, *Appl. Phys. Lett.* **108**, 252103

- (2016).
- [76] W. Jin, P.-C. Yeh, N. Zaki, D. Zhang, J. T. Liou, J. T. Sadowski, A. Barinov, M. Yablonskikh, J. I. Dadap, P. Sutter, I. P. Herman, and R. M. Osgood, Substrate interactions with suspended and supported monolayer MoS₂: Angle-resolved photoemission spectroscopy, *Phys. Rev. B* **91**, 121409 (2015).
- [77] T. Eknapakul, P. King, M. Asakawa, P. Buaphet, R.-H. He, S.-K. Mo, H. Takagi, K. Shen, F. Baumberger, T. Sasagawa, *et al.*, Electronic structure of a quasi-freestanding MoS₂ monolayer, *Nano letters* **14**, 1312 (2014).
- [78] R. Pisoni, A. Kormányos, M. Brooks, Z. Lei, P. Back, M. Eich, H. Overweg, Y. Lee, P. Rickhaus, K. Watanabe, T. Taniguchi, A. Imamoglu, G. Burkard, T. Ihn, and K. Ensslin, Interactions and Magnetotransport through Spin-Valley Coupled Landau Levels in Monolayer MoS₂, *Phys. Rev. Lett.* **121**, 247701 (2018).
- [79] H. C. Diaz, Y. Ma, S. Kolekar, J. Avila, C. Chen, M. C. Asensio, and M. Batzill, Substrate dependent electronic structure variations of van der Waals heterostructures of MoSe₂ or MoSe₂(1-x)Te_{2x} grown by van der Waals epitaxy, *2D Mater.* **4**, 025094 (2017).
- [80] N. R. Wilson, P. V. Nguyen, K. Seyler, P. Rivera, A. J. Marsden, Z. P. Laker, G. C. Constantinescu, V. Kandyba, A. Barinov, N. D. Hine, *et al.*, Determination of band offsets, hybridization, and exciton binding in 2D semiconductor heterostructures, *Sci. Adv.* **3**, e1601832 (2017).
- [81] S. Larentis, H. C. P. Movva, B. Fallahazad, K. Kim, A. Behroozi, T. Taniguchi, K. Watanabe, S. K. Banerjee, and E. Tutuc, Large effective mass and interaction-enhanced Zeeman splitting of K-valley electrons in MoSe₂, *Phys. Rev. B* **97**, 201407 (2018).
- [82] S. Ulstrup, J. Katoch, R. J. Koch, D. Schwarz, S. Singh, K. M. McCreary, H. K. Yoo, J. Xu, B. T. Jonker, R. K. Kawakami, A. Bostwick, E. Rotenberg, and C. Jozwiak, Spatially Resolved Electronic Properties of Single-Layer WS₂ on Transition Metal Oxides, *ACS Nano* **10**, 10058 (2016).
- [83] M. Dendzik, M. Michiardi, C. Sanders, M. Bianchi, J. A. Miwa, S. S. Grønberg, J. V. Lauritsen, A. Bruix, B. Hammer, and P. Hofmann, Growth and electronic structure of epitaxial single-layer WS₂ on Au(111), *Phys. Rev. B* **92**, 245442 (2015).

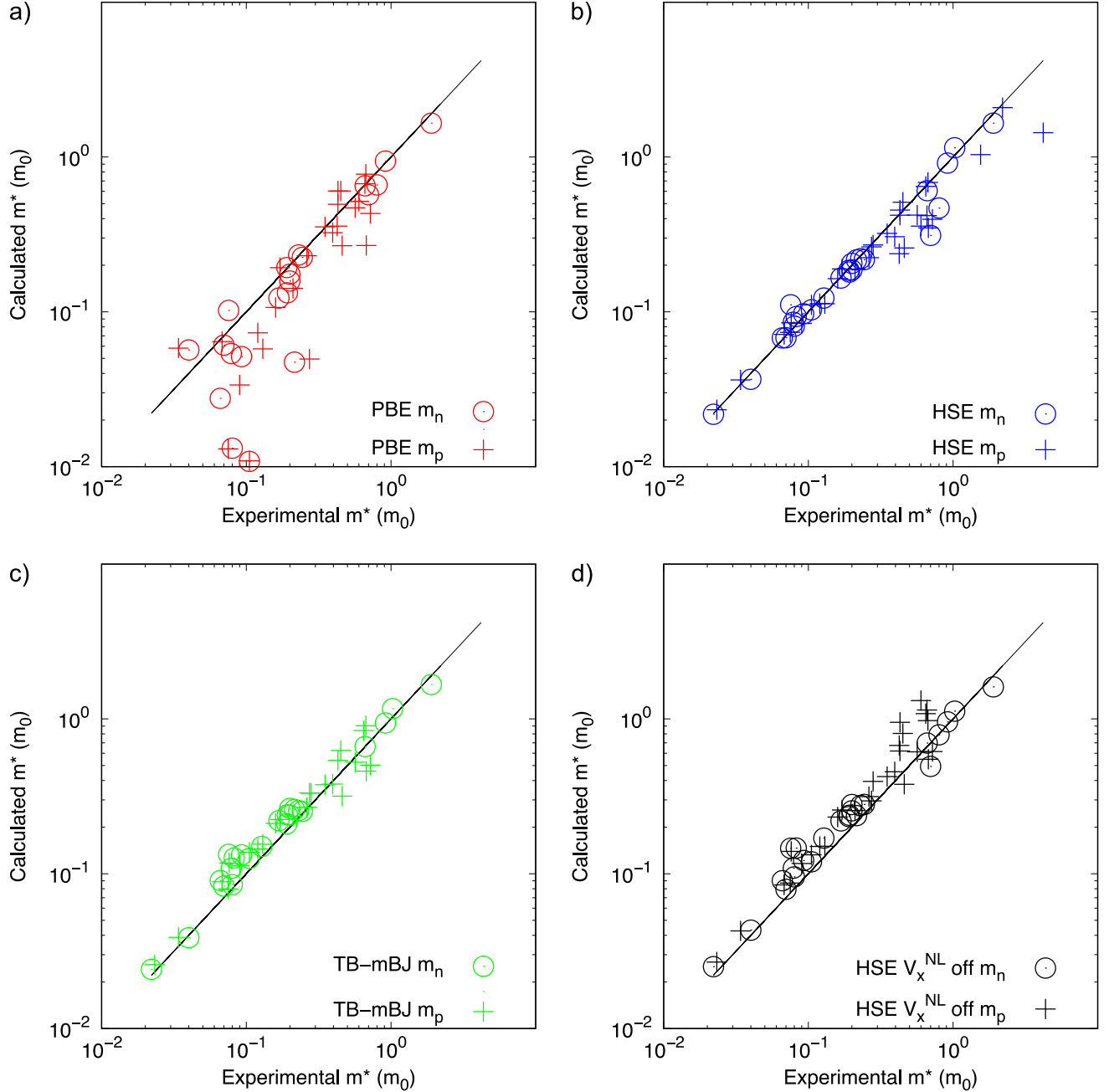


FIG. 1. Calculated versus experimental effective masses for the `mstar60` dataset. This figure provides a graphical overview of Table I. Circles are used for conduction band effective masses and cross symbols for valence band effective masses. Effective masses are calculated with the following exchange-correlation functionals/potentials: a) PBE, b) HSE06, c) TB-mBJ/LDA and d) HSE06 with the nonlocal exchange potential term V_x^{NL} switched off in the calculation of the matrix element. HSE-derived effective masses show the best agreement with experiment.

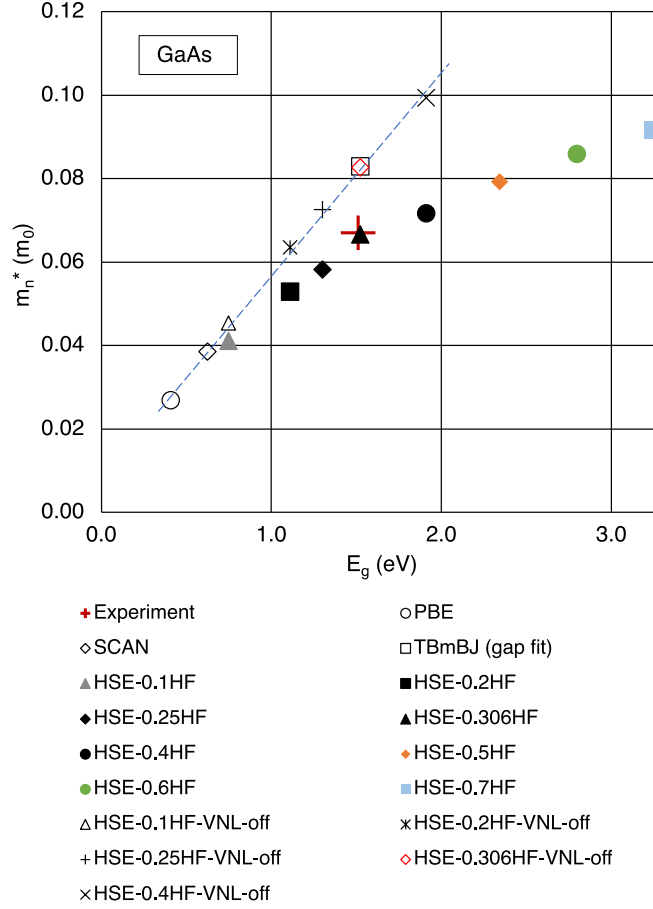


FIG. 2. Effective mass of the conduction band of GaAs at Γ versus the band gap for different settings of the exchange-correlation functional. There is a linear relationship between the effective mass and the band gap for all exchange-correlation functionals that do not include nonlocal exchange. Effective masses obtained from hybrid functionals considering nonlocal exchange deviate from that linear relationship. Only upon including nonlocal exchange, both the experimental band gap and experimental effective mass can be reproduced correctly in the calculation.

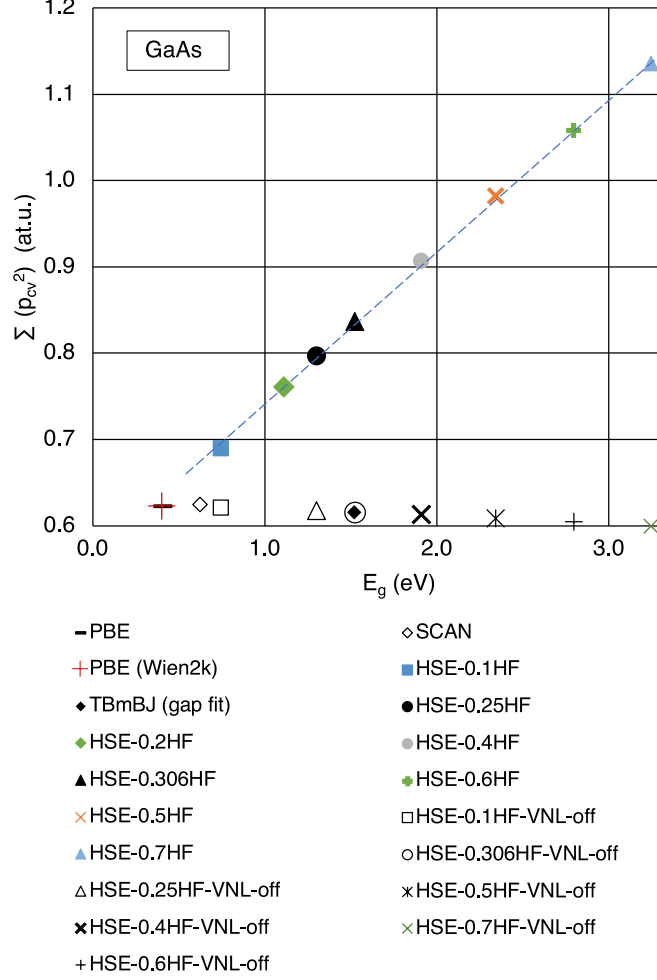


FIG. 3. Sum of the squared matrix element $|p_{cv}|^2$ (see Eq. (6)) versus the band gap for different settings of the exchange-correlation potential for the conduction band effective mass of GaAs at Γ . $\sum |p_{cv}|^2$ includes contributions from the transitions between the conduction band and the heavy-hole, light-hole and split-off valence bands. $\sum |p_{cv}|^2$ is roughly a constant for all exchange-correlation functionals that do not include nonlocal exchange, irrespective of the band gap. When the nonlocal exchange is considered via the V_x^{NL} term in the calculation of the matrix element, the sum increases with increasing HF proportion and increasing band gap. This graph shows the importance of including the nonlocal exchange on the HSE level for calculating accurate optical matrix elements.

TABLE I. Calculated and experimental effective masses m^* (m_0). m_n denote effective masses of the conduction band, m_p effective masses of the valence band. ‘hh’, ‘lh’ and ‘so’ stand for heavy hole, light hole and split-off band, respectively. Locations and directions in the Brillouin zone are indicated. The space group number of each material is given in parenthesis.

		experiment	PBE	HSE06	HSE06, V_x^{NL} off	TB-mBJ
Si (227)	$m_{n,\perp}$ (CBM)	0.191	0.193	0.185	0.234	0.210
	$m_{n,\parallel}$ (CBM)	0.916	0.943	0.913	0.957	0.942
	$m_{p,\text{hh}}$ (Γ) [100]	0.46 [68]	0.267	0.259	0.379	0.317
	$m_{p,\text{lh}}$ (Γ) [100]	0.171 [68]	0.193	0.189	0.258	0.224
	$m_{p,\text{so}}$ (Γ)	0.262	0.230	0.224	0.315	0.269
GaAs (216)	m_n (Γ)	0.066	0.028	0.068	0.090	0.090
	$m_{n,\perp}$ (X6)	0.23	0.233	0.220	0.276	0.255
	$m_{n,\parallel}$ (X6) ^{† a}	1.3	-0.534	-0.90	-1.016	-0.294
	$m_{n,\perp}$ (L6)	0.075	0.102	0.111	0.146	0.134
	$m_{n,\parallel}$ (L6)	1.9	1.656	1.654	1.609	1.671
	$m_{p,\text{hh}}$ (Γ) [100]	0.395	0.324	0.306	0.456	0.380
	$m_{p,\text{lh}}$ (Γ) [100]	0.09	0.034	0.084	0.117	0.113
	$m_{p,\text{so}}$ (Γ)	0.16	0.107	0.164	0.233	0.212
GaN (186)	$m_{n,\parallel}$ (Γ)	0.2	0.158	0.186	0.255	0.240
	$m_{n,\perp}$ (Γ)	0.2	0.175	0.206	0.280	0.264
InP (216)	m_n (Γ)	0.079	0.054	0.086	0.109	0.108
	$m_{p,\text{hh}}$ (Γ) [100]	0.565	0.469	0.422	0.612	0.525
	$m_{p,\text{lh}}$ (Γ) [100]	0.12	0.073	0.113	0.150	0.145
	$m_{p,\text{so}}$ (Γ)	0.21 [69]	0.142	0.189	0.256	0.236

^a excluded from the statistical analysis

TABLE I. (continued)

		experiment	PBE	HSE06	HSE06, V_x^{NL} off	TB-mBJ
CdS (186)	$m_{n,\perp}$ (Γ , A exciton)	0.192	0.133	0.181	0.239	0.242
	$m_{n,\parallel}$ (Γ , A exciton)	0.168	0.123	0.165	0.220	0.220
	$m_{p,\perp}$ (Γ , A exciton)	0.675	0.268	0.348	0.549	0.463
	$m_{p,\parallel}$ (Γ , A exciton) ^{† a}	5	0.993	0.827	1.57	1.57
CdTe (216)	m_n (Γ)	0.093	0.051	0.097	0.122	0.133
	$m_{p,\text{lh}}$ [100] (Γ)	0.13	0.058	0.113	0.150	0.155
	$m_{p,\text{hh}}$ [100] (Γ)	0.72	0.431	0.396	0.615	0.503
PbS (225)	$m_{n,\perp}$ (L)	0.08	0.013	0.081	0.096	0.085
	$m_{n,\parallel}$ (L)	0.105	0.011	0.103	0.119	0.126
	$m_{p,\perp}$ (L)	0.075	0.013	0.074	0.087	0.080
	$m_{p,\parallel}$ (L)	0.105	0.011	0.111	0.132	0.138
PbSe (225)	$m_{n,\perp}$ (L)	0.04	0.057	0.037	0.043	0.039
	$m_{n,\parallel}$ (L)	0.07	0.061	0.068	0.079	0.083
	$m_{p,\perp}$ (L)	0.034	0.058	0.036	0.043	0.039
	$m_{p,\parallel}$ (L)	0.068	0.064	0.071	0.085	0.089
PbTe (225)	$m_{n,\perp}$ (L)	0.022	0.003	0.022	0.025	0.024
	$m_{n,\parallel}$ (L)	0.215	0.047	0.216	0.237	0.260
	$m_{n,\perp}$ (L)	0.023	0.003	0.023	0.027	0.026
	$m_{p,\parallel}$ (L)	0.273	0.050	0.263	0.296	0.332
SiC (216)	$m_{n,\parallel}$ (X)	0.662	0.652	0.606	0.698	0.664
	$m_{n,\perp}$ (X)	0.244	0.225	0.217	0.281	0.253
	m_p (Γ) [100]	0.45 ^b	0.603	0.510	0.805	0.625
BN [70] (194)	m_p (\bar{K} , $\bar{\Gamma}$ - \bar{K} direction) ^{† c}	0.49 [71]	0.971	0.775	1.515	1.185

^a excluded from the statistical analysis^b specifics of the valence band and direction of the experimentally obtained effective mass are unclear^c excluded from the statistical analysis

TABLE I. (continued)

		experiment	PBE	HSE06	HSE06, V_x^{NL} off	TB-mBJ
bP (64)	m_n (Y) [010]	1.027 [72]	—	1.15	1.12	1.17
	m_n (Y) [001]	0.128 [72]	—	0.123	0.170	0.150
	m_n (Y) [100]	0.083 [72]	—	0.093	0.146	0.126
	m_p (Y) [010]	0.648 [72]	—	0.646	1.08	0.842
	m_p (Y) [001]	0.28 [72]	—	0.270	0.395	0.332
	m_p (Y) [100]	0.076 [72]	—	0.085	0.140	0.117
MoS ₂ [73] (194)	m_p ($\bar{\Gamma}$, $\bar{\Gamma}$ - \bar{K} direction)	0.67 [74]	0.774 ^a	0.685	0.976	0.904
WS ₂ (194)	m_p (\bar{K} , $\bar{\Gamma}$ - \bar{K} direction)	0.35 [75]	0.354 ^b	0.321	0.424	0.376
	$m_{p,\text{VB}-1}$ (\bar{K} , $\bar{\Gamma}$ - \bar{K} direction)	0.43 [75]	0.495 ^c	0.454	0.620	0.539
1L MoS ₂	m_p (Γ , Γ -K direction)	2.2 [74, 76]	— ^d	2.084 ^e	— ^f	—
	m_p (K, Γ -K direction)	0.52 [76, 77]	0.603 ^g	0.421 ^h	0.951	—
	m_n (K)	0.69 [77, 78]	0.402 ⁱ	0.312 ^j	0.494	—
1L MoSe ₂	m_p (K, Γ -K direction)	0.66 [54, 79, 80]	0.672 ^k	0.418	1.141	—
	m_n (K)	0.8 [81]	0.468 ^l	0.333	0.584	—
1L WS ₂	m_p ($\bar{\Gamma}$, $\bar{\Gamma}$ - \bar{K} direction)	1.55 [82]	— ^m	1.04	— ⁿ	—
	m_p (\bar{K} , $\bar{\Gamma}$ - \bar{K} direction)	0.425 [82, 83]	0.358 ^o	0.237	0.674	—
	$m_{p,\text{so}}$ (\bar{K} , $\bar{\Gamma}$ - \bar{K} direction)	0.6 [82, 83]	0.517 ^p	0.358	1.31	—
1L WSe ₂	m_p (Γ , Γ -K direction)	4.2 [80]	— ^q	1.436	— ^r	—

^a Perturbation theory (PT) result has an error of 14% with respect to the band curvature fit

^b PT result has an error of 5% with respect to the band curvature fit

^c PT result has an error of 7% with respect to the band curvature fit

^d Converged PT result could not be obtained. The band curvature fit gives an effective mass of 3.73 m_0

^e Perturbation theory result has an error of 13% with respect to the band curvature fit

^f Converged PT result could not be obtained

^g PT result has an error of 15% with respect to the band curvature fit

^h PT result has an error of 10% with respect to the band curvature fit

ⁱ PT result has an error of 7% with respect to the band curvature fit

^j PT result has an error of 8% with respect to the band curvature fit

^k PT result has an error of 16% with respect to the band curvature fit

^l PT result has an error of 8% with respect to the band curvature fit

^m Converged PT result could not be obtained. The band curvature fit gives an effective mass of 2.93 m_0

ⁿ Converged PT result could not be obtained.

^o PT result has an error of 5% with respect to the band curvature fit

^p PT has an error of 8% with respect to the band curvature fit

^q Converged PT result could not be obtained. The band curvature fit gives an effective mass of 4.46 m_0

^r Converged PT result could not be obtained.

TABLE II. Summary statistics for the error in the calculated effective mass for the bulk materials of the `mstar60` dataset. The statistics include 42 effective masses of 13 materials.

	PBE	HSE06	HSE06, V_x^{NL} off	TB-mBJ
ME (m_0)	-0.053	-0.034	0.036	0.013
MAE (m_0)	0.075	0.043	0.065	0.054
STDE (m_0)	0.100	0.090	0.100	0.080
MRE (%)	-27	-4.7	22	16
MARE (%)	38	10	26	21
STDRE (%)	40	16	22	21